

Numerical solution scheme for inert, disperse, and dilute gas-particle flows

J.S. Sachdev, C.P.T. Groth ^{*}, J.J. Gottlieb

University of Toronto Institute for Aerospace Studies, 4925 Dufferin Street, Toronto, Ont., Canada M3H 5T6

Received 24 April 2006; received in revised form 28 August 2006

Abstract

A multi-velocity formulation is proposed for the solution of an Eulerian representation of an inert, disperse, and dilute particle-phase of a gas-particle flow. Single-velocity formulations are capable of predicting regions of zero particle concentration but are problematic with crossing particle trajectories or compression waves. The multi-velocity formulation described here can account for crossing particle trajectories by splitting the particle-phase into distinct velocity families which are transported separately in the flow. Switching of the particle families at solid boundaries and due to momentum transfer with the gas-phase is conducted in a manner that enforces conservation of mass, momentum, and energy. This numerical method is combined with a parallel block-based adaptive mesh refinement algorithm that is very effective in treating problems with disparate length scales. The block-based data structure lends itself naturally to domain decomposition and thereby enables efficient and scalable implementations of the algorithm on distributed-memory multi-processor architectures. Numerical results are described to demonstrate the capabilities of the approach for predicting gas-particle flows.

© 2006 Elsevier Ltd. All rights reserved.

Keywords: Inert; Disperse; Dilute gas-particle flow; Adaptive mesh refinement

1. Introduction and motivation

Both Lagrangian and Eulerian formulations are commonly used in the scientific community when treating the motion of an inert (non-reacting), dilute (negligible volume fraction), and disperse (negligible particle–particle collisions) particle-phase coupled with a fluid. As a consequence of the assumptions of an inert and dilute particle-phase, there is no interaction between the phases due to mass transfer or volume effects. However, interaction between the phases occurs due to momentum (drag) and heat transfer caused by the collisions between the solid particles and the gas molecules. This collision process tends to relax the system into an equilibrium state in which the two phases are of an equal velocity and temperature.

^{*} Corresponding author. Tel.: +1 416 667 7715; fax: +1 416 667 7799.
E-mail address: groth@utias.utoronto.ca (C.P.T. Groth).

In a Lagrangian formulation, the trajectories of individual particles are tracked (see for example the work by Najjar et al. (2000) and Patankar and Joseph (2001a,b)). A set of ordinary differential equations is used to track the translational and rotational motion of the particle as well as the particle's temperature. Although conceptually straight-forward to implement, Lagrangian methods can be prohibitively expensive since a large number of particles is required to achieve a realistic concentration of particles with a distribution of characteristics (such as mass, diameter, and specific heat). Ad hoc puff models, where simulated particles represent a cloud of actual particles, are often employed to enable simulations with realistic concentrations.

In an Eulerian formulation the particle-phase is treated as a continuum and a set of partial differential equations representing the conservation of mass (concentration), momentum, and energy is used to govern the motion of the particle-phase (Saurel et al., 1994; Slater and Young, 2001; Saito et al., 2003; Igra et al., 2004). The Eulerian framework can readily cope with particles having a distribution of sizes and characteristics. This can be accomplished by considering multiple families of different particles, each with their own mass, momentum, and energy. A set of governing equations is then required for each particle family. It has been well-established that the set of partial differential equations governing dilute and disperse particle flow is both hyperbolic and degenerate (Saurel et al., 1994; Slater and Young, 2001; Sauerwein and Fendell, 1965). The degeneracy is a direct result of the assumptions that the particle volume fraction is negligible (dilute) and that the effects of inter-particle collisions are not important (disperse). The lack of particle collisions means that there are no normal surface forces produced by the random motion of the particles themselves and hence there is no pressure-like term (or viscous-like term) in the particle momentum and energy equations. Physically, the main implications of the degeneracy are twofold. First, particle vacuums can exist as there are no direct pressure forces to drive the particles from regions of high concentrations to those with lower concentrations. Moreover, as interactions between particles have been neglected, the paths of particles can cross. Faster moving particles can freely over-take and pass slower moving particles without being subject to any particle-particle interaction forces.

From a mathematical perspective, the degenerate nature of the gas-particle flow equations must be accounted for when designing a numerical scheme for their solution. Although, Lagrangian modelling methods can readily deal with particle trajectories that cross, Eulerian finite-volume methods can produce inaccurate and physically incorrect numerical solutions. This is a result of insufficient characteristic fields from which to reconstruct the solution and therefore solution information and accuracy can be lost. The solution of the particle-phase Riemann problem proposed by Saurel et al. (1994) allows for particle vacuums and for particle paths to cross, however, flows involving the compression of the particle-phase, such as at reflection boundary conditions, are problematic. In their paper, Saurel et al. discussed but did not pursue a multi-velocity treatment of the particle-phase, in which the particle-field is split up into distinct velocity families and are advected separately in the flow. Though this method requires additional computing resources in terms of both memory and computing time, particle compression waves are permitted and, therefore, crossing trajectories and reflection boundary conditions can be more realistically modelled.

The design and implementation of a multi-velocity formulation of the particle-phase is the topic of the current paper. For two-dimensional flow, the particle-phase is decomposed into four distinct velocity families, with velocities in the four quadrants of velocity space associated with particles travelling in the north-east, north-west, south-west, and south-east directions. Each particle family is treated separately. The flux of the particle-phase at cell interfaces is then determined using a simplified version of the Riemann solution defined by Saurel et al. (1994). Switching of the particle velocity families at solid boundaries and due to momentum transfer with the gas-phase is conducted in a manner that enforces conservation of mass, momentum, and energy.

The organization of the paper is as follows. The governing equations for an Eulerian formulation of an inviscid gas-particle flow are reviewed in the next section and the numerical algorithm is described in the following section. An eigenanalysis and a dispersion analysis of the one-dimensional form of the gas-particle flow equations are conducted to gain the necessary insight into the wave structure and dynamic behaviour of the system equations required for constructing an algorithm for their numerical solution. A cell-centred upwind finite-volume scheme is proposed for the solution of the governing equations. Both single-velocity and multi-velocity particle-phase formulations are discussed. The finite-volume scheme has been developed in coordination with a block-based adaptive mesh refinement (AMR) algorithm that automatically adapts

the computational grid to the solution of the governing equations and can be very effective in treating problems with disparate length scales. In addition, this block-based data structure lends itself naturally to domain decomposition and has thereby enabled efficient and scalable implementations of the algorithm on distributed-memory multi-processor architectures. The AMR scheme and the parallel implementation are also discussed in this section. Finally, numerical test cases are described to demonstrate the validity and capabilities of the multi-velocity formulation.

2. Governing equations of motion

2.1. Governing equations of motion

The equations used herein to describe the motion of a coupled gas-particle flow are now reviewed (Marble, 1970; Rudinger, 1980). The compressible Euler equations are used to model the motion of the calorically perfect gas-phase and an Eulerian formulation is used to govern the behaviour of the inert, dilute, and disperse particle-phase that is presented here for N particle families. Each particle family can have distinct sizes and characteristics and has its own mass, momentum, and energy. The conservation of mass (continuity equation) for the gas and particle-phases are given by

$$\frac{\partial \rho}{\partial t} + \nabla \cdot (\rho \vec{v}) = 0, \quad (1)$$

$$\frac{\partial \sigma_{p_i}}{\partial t} + \nabla \cdot (\sigma_{p_i} \vec{u}_i) = 0 \quad \text{for } i = 1, \dots, N, \quad (2)$$

where ρ and \vec{v} are the gas-phase density and velocity, and σ_{p_i} and \vec{u}_i are the particle-phase concentration and velocity for the i th particle family.

A strong interaction can exist between the relatively heavy solid particles and the gas due to momentum transfer (drag) between the two phases. The conservation of momentum for the gas and particle phases are given by

$$\frac{\partial}{\partial t} (\rho \vec{v}) + \nabla \cdot (\rho \vec{v} \vec{v} + p \vec{\mathbf{I}}) = - \sum_{i=1}^N \frac{\sigma_{p_i}}{\tau_{v_i}} (\vec{v} - \vec{v}_i), \quad (3)$$

$$\frac{\partial}{\partial t} (\sigma_{p_i} \vec{u}_i) + \nabla \cdot (\sigma_{p_i} \vec{u}_i \vec{u}_i) = \frac{\sigma_{p_i}}{\tau_{v_i}} (\vec{v} - \vec{v}_i) \quad \text{for } i = 1, \dots, N, \quad (4)$$

where $\vec{\mathbf{I}}$ is the unit dyad and p is the gas-phase pressure. The momentum (drag) transfer term has been written in terms of a relaxation time, τ_v given by

$$\tau_v = \frac{m_p G}{3\pi d_p \mu f(Re_p)}, \quad (5)$$

where the particles are assumed to be spherical and rigid. Particle–particle interactions on drag are neglected. The function $f(Re_p)$ is a non-linear correction that extends Stokes drag law, for which $f(Re_p) = 1$, for single particles to higher slip Reynolds numbers. The drag law can be written as

$$C_D = \frac{24}{Re_p} f(Re_p) = \frac{24}{Re_p} \left(1 + d_1 Re_p^{d_2} + \frac{Re_p}{24} \frac{d_3}{1 + d_4/Re_p^{d_5}} \right), \quad (6)$$

where the coefficients for five drag laws are listed in Table 1. The first set of coefficients correspond to Stokes drag, which is valid for very low slip Reynolds numbers. The Klyachko–Putnam drag law extends Stokes drag to moderate slip Reynolds numbers (Rudinger, 1980). The Turton and Levenspiel (1986) and Haider and Levenspiel (1989) drag laws are valid for slip Reynolds numbers up to one-hundred thousand, $Re_p < 10^5$.

If the particle size is small or comparable to the mean free path of the fluid, λ , then the assumption of a continuum flow around the particle is invalid. In this regime, the drag laws will over predict the drag force on the particle. A correction factor, known as the Cunningham correction, G , is included in Eq. (5) to account for this effect (Rudinger, 1980) as is given by

Table 1
Coefficients for various drag laws

	d_1	d_2	d_3	d_4	d_5
Stokes (Rudinger, 1980)	0	0	0	0	0
Oseen (Rudinger, 1980)	3/16	1	0	0	0
Klyachko–Putnam (Rudinger, 1980)	1/6	2/3	0	0	0
Turton and Levenspiel (1986)	0.173	0.657	0.413	16300	1.09
Haider and Levenspiel (1989)	0.1806	0.6459	0.4251	6880.95	1

$$G = 1 + Kn \left[2.492 + 0.84 \exp \left(-\frac{1.74}{Kn} \right) \right], \tag{7}$$

where Kn is the Knudsen number which is defined as $Kn = \lambda/d_p$. This correction factor increases the momentum transfer relaxation time which leads to a decreased drag force.

The gas-phase is taken to be calorically perfect and the total energies of the two phases are given by

$$E = \frac{p}{(\gamma - 1)} + \frac{1}{2} \rho \vec{v} \cdot \vec{v} = \rho c_v T + \frac{1}{2} \rho \vec{v} \cdot \vec{v}, \tag{8}$$

$$E_{p_i} = \sigma_{p_i} c_{m_i} T_{p_i} + \frac{1}{2} \sigma_{p_i} \vec{u}_i \cdot \vec{u}_i, \tag{9}$$

where $\gamma = c_p/c_v$ is the ratio of the specific heats for the gas, p is the gas-phase pressure, c_{m_i} is the specific heat of i th particle family, and T_{p_i} is the i th particle-phase temperature. The ideal gas law provides a relationship between the gas pressure, p , and temperature, T , $p = \rho RT = \rho a^2/\gamma$ where $a = \sqrt{\gamma RT}$ is the sound speed and R is the gas constant. The conservation of energy for the gas and solid particle-phases can be expressed in terms of their total energies per unit mass by

$$\frac{\partial E}{\partial t} + \nabla \cdot [\vec{v}(E + p)] = - \sum_{i=1}^N \left[\frac{\sigma_{p_i}}{\tau_{v_i}} (\vec{v} - \vec{u}_i) \cdot \vec{u}_i + \frac{\sigma_{p_i} c_p}{\tau_{T_i}} (T - T_{p_i}) \right], \tag{10}$$

$$\frac{\partial E_{p_i}}{\partial t} + \nabla \cdot (\vec{u}_i E_{p_i}) = \frac{\sigma_{p_i}}{\tau_{v_i}} (\vec{v} - \vec{u}_i) \cdot \vec{u}_i + \frac{\sigma_{p_i} c_p}{\tau_{T_i}} (T - T_{p_i}) \quad \text{for } i = 1, \dots, N. \tag{11}$$

The rate of heat transfer between the phases depends on the instantaneous temperature difference (Rudinger, 1980). Igra et al. (2004) observed that due to the lack of the pressure-like term in the particle-phase, the particle-phase total energy equation can be simplified into a thermal energy equation while maintaining a conservative form by subtracting the particle-phase continuity and momentum equations from it. The particle-phase thermal energy equation is

$$\frac{\partial \epsilon_{p_i}}{\partial t} + \nabla \cdot (\vec{u}_i \epsilon_{p_i}) = \frac{\sigma_{p_i} c_p}{\tau_{T_i}} (T - T_{p_i}) \quad \text{for } i = 1, \dots, N, \tag{12}$$

where $\epsilon_{p_i} = \sigma_{p_i} c_{m_i} T_{p_i}$ is the particle-phase total thermal energy for the i th family.

The relaxation time associated with the heat transfer, τ_T , is given by

$$\tau_T = \frac{m_p c_p}{2\pi d_p \kappa Nu}, \tag{13}$$

where κ is the thermal conductivity of the gas and Nu is the Nusselt number which accounts for increase in heat transfer due to convection (Rudinger, 1980). For a single particle, the Nusselt number can be expressed in terms of the slip Reynolds number and the Prandtl number, $Pr = \mu c_p/\kappa$, as

$$Nu = 1 + 0.3 Pr^{1/3} Re_p^{1/2}. \tag{14}$$

Note that the ratio of the relaxation times, Eqs. (5) and (13), can be related to the Prandtl number, Pr , by $\tau_T/\tau_v = \frac{3}{2} Pr$ when the non-linear drag correction, Cunningham correction, and convective heat transfer are ignored.

2.2. Eigenanalysis

Eqs. (2), (4) and (12) provide an Eulerian description for the particle-phase and are very similar to the Euler equations for inviscid, compressible gases with the exception of a pressure-like term in the particle-phase momentum or energy equations. This feature is a direct result of the assumption that the particle-phase is disperse. The lack of particle–particle collisions means that there are no normal surface forces produced by the random motion of the particles themselves and hence there are no pressure-like term (or viscous-like term) in the particle momentum and energy equations. The eigenstructure of the one-dimensional form of the preceding two-phase flow equations is now considered in order to gain an understanding of the influence that the absence of a particle pressure has on the unsteady wave structure of this system of equations before pursuing a numerical solution.

The one-dimensional, weak conservation form of the governing equations in the case of a single-family mono-sized particle-phase can be summarized by

$$\frac{\partial \mathbf{U}}{\partial t} + \frac{\partial}{\partial x} \mathbf{F}(\mathbf{U}) = \mathbf{P}(\mathbf{U}), \quad (15)$$

where $\mathbf{U} = [\rho, \rho v, E, \sigma_p, \sigma_p u, \epsilon_p]^T$ is the one-dimensional flow state vector of conserved variables, $\mathbf{F}(\mathbf{U})$ is the flux vector, and $\mathbf{P}(\mathbf{U})$ is the phase-interaction source vector. In the “frozen” limit, the characteristic times scales of the particle drag and heat transfer, τ_v and τ_T , are assumed to be large relative to the propagation times associated with the unsteady wave motion such that the phase-interaction terms can be neglected. In this limit, the equations governing the gas and particle-phases decouple. An eigenanalysis of the system in the frozen limit yields the set of real eigenvalues, λ_k ,

$$\lambda_1 = v - a, \quad \lambda_2 = v, \quad \lambda_3 = v + a, \quad \lambda_{4,5,6} = u \quad (16)$$

indicating the hyperbolic nature of the equations. The first three eigenvalues correspond to the well known acoustic and convective eigenvalues of the Euler equations. The last three repeated eigenvalues are associated with the particle-phase. The right eigenvectors corresponding to the frozen-limit eigenvalues are

$$(\vec{r}_1, \vec{r}_2, \vec{r}_3, \vec{r}_4, \vec{r}_5) = \begin{bmatrix} 1 & 1 & 1 & 0 & 0 \\ -a/\rho & 0 & a/\rho & 0 & 0 \\ a^2 & 0 & a^2 & 0 & 0 \\ 0 & 0 & 0 & 1 & 0 \\ 0 & 0 & 0 & 0 & 0 \\ 0 & 0 & 0 & 0 & 1 \end{bmatrix}. \quad (17)$$

This is an incomplete set of eigenvectors as only five linearly independent eigenvectors can be found for the six characteristic fields. One eigenvector associated with the $\lambda = u$ eigenvalue is missing. Because of this degeneracy in the eigensystem, the set of hyperbolic conservation equations governing disperse gas-particle flows is said to form a degenerate hyperbolic set, a result confirmed in the literature (Saurel et al., 1994; Slater and Young, 2001; Sauerwein and Fendell, 1965). The degeneracy is a direct result of the assumptions that the particle volume fraction is negligible (dilute) and that the effects of inter-particle collisions are not important (disperse). Physically, the main implications of the degeneracy are twofold. First, particle vacuums can exist as there are no direct pressure forces to drive the particles from regions of high concentrations to those with lower concentrations. Moreover, as interactions between particles have been neglected, the paths of particles can cross. Faster moving particles can freely over-take and pass slower moving particles without being subject to any particle–particle interaction forces.

2.3. Dispersion analysis

A linear dispersion analysis for initial value problems can be used to provide a better understanding of the dynamic behaviour and wave structure of the coupled gas-particle flow equations. In particular, an analysis of initial value problems for the linearized one-dimensional form of these equations is considered here. Marble

conducted a linear dispersion analysis of the boundary value problem for the same system of equations (Marble, 1970). The analysis of the equilibrium, frozen, and non-equilibrium dispersion relationships follows the procedure outlined by Groth et al. (1995).

The dispersive wave properties of the one-dimensional form of the gas-particle flow equations given by (15) can be assessed by considering the linearized primitive form of these equations given by

$$\frac{\partial \mathbf{W}}{\partial t} + \mathbf{A}_0 \frac{\partial \mathbf{W}}{\partial x} = \mathbf{Q}_0 \mathbf{W}, \tag{18}$$

where $\mathbf{W} = [\rho, v, T, \sigma_p, u, T_p]^T$ is the primitive solution vector and the matrices \mathbf{A}_0 and \mathbf{Q}_0 are the linearized coefficient matrices of the flux and phase-interaction source vectors determined by linearizing the primitive form of the equations about a quiescent (stationary) equilibrium state $\mathbf{W}_0 = [\rho_0, 0, T_0, \sigma_{p0}, 0, T_0]^T$. For initial value problems having solutions of the form $\mathbf{W} = \exp[i(\omega t - \xi x)]$, the differential wave operator for the linearized equations is defined by the eigenvalue problem given by $[i\omega \mathbf{I} - i\xi \mathbf{A}_0 - \mathbf{Q}_0] \mathbf{W} = 0$ where the temporal frequency, ω , can have real and imaginary components, $\omega = \omega_R + i\omega_I$, whereas the spatial frequency, ξ , is restricted to be real valued. The parameter, ξ , defines the frequency content of the linearized solution, which varies from the low frequencies for near equilibrium solutions to high frequencies for non-equilibrium solutions approaching the frozen limit. The condition for the stability of the solutions is $\omega_I > 0$.

In the equilibrium limit ($\tau_p, \tau_T \rightarrow 0$), the particles and gas are driven by the drag forces and heat transfer to move with the same velocity ($\vec{u} = \vec{v}$) and have the same temperature ($T_p = T$). An equilibrium density can be defined by setting $\bar{\rho} = \rho + \sigma_p = \rho(1 + \chi)$ where $\chi = \sigma_p/\rho$ is the particle loading factor and is constant for uniformly distributed particles. The system of equations in the equilibrium limit can then be reduced to three variables, in terms of the primitive variables $\bar{\rho}$, v , and T . In this case, the linearized non-dimensional coefficient matrix is given by

$$\mathbf{A}_0 = \begin{bmatrix} 0 & 1 & 0 \\ \bar{R}_0 T_0 / a_0^2 & 0 & \bar{R}_0 T_0 / a_0^2 \\ 0 & \bar{R}_0 / \bar{c}_{v0} & 0 \end{bmatrix}, \tag{19}$$

where T_0 is the temperature of the quiescent equilibrium state, $a_0 = \sqrt{\gamma R T_0}$ is the sound-speed of the quiescent equilibrium state and is used as a reference velocity in the dispersion analysis, the equilibrium gas constant and specific heat ratios are given by $\bar{R}_0 = \bar{c}_{p0} - \bar{c}_{v0} = R/(1 + \chi_0)$, $\bar{c}_{v0} = (c_v + \chi_0 c_m)/(1 + \chi_0)$, $\bar{c}_{p0} = (c_p + \chi_0 c_m)/(1 + \chi_0)$, and $\bar{\gamma}_0 = \bar{c}_{p0} / \bar{c}_{v0}$. The parameter χ_0 is the loading ratio of the reference equilibrium state. The solution of the eigenvalue problem, with $\lambda = \omega/\xi$, provides the equilibrium dispersion relationship

$$-\lambda[\lambda^2 - \bar{a}^2/a_0^2] = 0, \tag{20}$$

where $\bar{a} = \sqrt{\bar{\gamma}_0 \bar{R}_0 T_0}$ is the mixture sound-speed. Determination of the roots of this polynomial gives the following non-dimensional equilibrium wave speeds

$$\lambda_1 = -\bar{a}/a_0 = -\sqrt{\bar{\gamma}_0/\gamma}, \quad \lambda_2 = 0, \quad \lambda_3 = \bar{a}/a_0 = \sqrt{\bar{\gamma}_0/\gamma}. \tag{21}$$

In the equilibrium limit, the imaginary part of the wave-speed is zero, $\lambda_I = 0$, which corresponds to non-dissipative, coherent wave propagation.

Now consider the linearized equations in the high-frequency or frozen limit. The linearized and non-dimensionalized coefficient and source Jacobians are

$$\mathbf{A}_0 = \begin{bmatrix} 0 & 1 & 0 & 0 & 0 & 0 \\ RT_0/a_0^2 & 0 & RT_0/a_0^2 & 0 & 0 & 0 \\ 0 & R/c_v & 0 & 0 & 0 & 0 \\ 0 & 0 & 0 & 0 & 1 & 0 \\ 0 & 0 & 0 & 0 & 0 & 0 \\ 0 & 0 & 0 & 0 & 0 & 0 \end{bmatrix}, \quad \mathbf{Q}_0 = \frac{t_0}{\tau_T} \begin{bmatrix} 0 & 0 & 0 & 0 & 0 & 0 \\ 0 & -\frac{3}{2}\chi_0 Pr & 0 & 0 & \frac{3}{2}\chi_0 Pr & 0 \\ 0 & 0 & -\gamma\chi_0 & 0 & 0 & \gamma\chi_0 \\ 0 & 0 & 0 & 0 & 0 & 0 \\ 0 & \frac{3}{2}Pr & 0 & 0 & -\frac{3}{2}Pr & 0 \\ 0 & 0 & c_p/c_m & 0 & 0 & -c_p/c_m \end{bmatrix}. \tag{22}$$

In the frozen limit, the characteristic time scales of the viscous drag and heat transfer terms, τ_v and τ_T , are assumed to be large relative to the differences in velocity and temperature such that the source matrix \mathbf{Q}_0 can be neglected. The dispersion relationship in the frozen limit is found by solving

$$\det(\lambda \mathbf{I} - \mathbf{A}_0) = -\lambda^4[\lambda^2 - 1] = 0, \quad (23)$$

where $\lambda = \omega/\xi$. The solution of this polynomial equation yields the non-dimensional frozen wave speeds

$$\lambda_1 = -1, \quad \lambda_{2,4,5,6} = 0, \quad \lambda_3 = 1. \quad (24)$$

As in the near-equilibrium limit, the wave-speeds in the frozen limit show non-dissipative, coherent wave propagation since $\lambda_i = 0$ for each wave, including the four convective waves (three associated with the particle-phase) and two acoustic waves (associated with the gas-phase).

The dispersion relationship for the general non-equilibrium system can be determined by solving the eigenvalue problem for the characteristic wave-speeds, $[\omega \mathbf{I} - i\xi \mathbf{A}_0 - \mathbf{Q}_0] \mathbf{W} = 0$. The resulting dispersion relationship is

$$\lambda^2(\lambda^4 - ic_3\lambda^3 - c_2\lambda^2 + ic_1\lambda + c_0) = 0, \quad (25)$$

where $\lambda = \omega/\xi$. The spatial frequency, ξ , can be expressed as $\xi = 2\pi x_0/L = a_0 t_0/a_0 \tau = t_0/\tau$, where t_0 is a reference time scale and $L = a_0 \tau$ is the wavelength of the solution. The frozen and equilibrium limits are defined by high and low frequency solution limits (i.e., $\tau \rightarrow 0$ and $\tau \rightarrow \infty$, respectively). The coefficients c_3 , c_2 , c_1 , and c_0 are given by

$$\begin{aligned} c_3 &= \tilde{\tau}(1 + \chi_0) \left(\gamma \frac{\overline{c_{v0}}}{c_m} + \frac{3}{2} Pr \right), \\ c_2 &= 1 + \tilde{\tau}^2 \left(\frac{3}{2} Pr \gamma (1 + \chi_0)^2 \frac{\overline{c_{v0}}}{c_m} \right), \\ c_1 &= \tilde{\tau} \left(\frac{3}{2} Pr + (1 + \chi_0) \frac{\overline{c_{p0}}}{c_m} \right), \\ c_0 &= \tilde{\tau}^2 \left(\frac{3}{2} Pr (1 + \chi_0) \frac{\overline{c_{p0}}}{c_m} \right), \end{aligned}$$

where $\tilde{\tau} = \tau/\tau_T$ is a non-dimensional relaxation time-scale. In the general non-equilibrium case, the non-dimensional wave speeds, λ , can have real and imaginary components, $\lambda = \lambda_R + i\lambda_I$, characteristic of dispersive wave propagation. Analytic expressions for the non-dimensional wave speeds cannot be found; however, it is instructive to investigate the dispersion relationship for the non-equilibrium system by numerically calculating the waves speeds as a function of the solution frequency as controlled by $\tilde{\tau}$. The coefficients of the non-equilibrium dispersion relationship are functions of various non-dimensional numbers: Pr , χ_0 , γ , $\overline{c_{p0}}/c_m$, and $\overline{c_{v0}}/c_m$. The ratio of the equilibrium specific heat at constant pressure and volume with respect to the specific heat of the non-reacting particle, $\overline{c_{p0}}/c_m$ and $\overline{c_{v0}}/c_m$, are dependent on the gas-type, particle material, and the particle loading factor of the quiescent equilibrium state whereas the ratio of the gas-phase specific heats is dependent only on the gas. For the purpose of the current analysis, calorically perfect air, $(\gamma, c_p) = (1.4, 1004.72 \text{ J/kg K})$ at a density and temperature of 1.0 kg/m^3 and 300 K , respectively, and glass beads, $c_m = 840 \text{ J/kg K}$, were chosen to represent the physical properties of the gas and particle-phases. The effect of the frequency content of the linearized solution on the dispersive wave behaviour was then investigated for various loading factors, χ_0 and Prandtl numbers, Pr .

Three loading factors were chosen for this analysis: $\chi_0 = 0.1, 0.5$, and 1 . The particle volume fraction at the maximum loading factor is 4.2×10^{-4} which corresponds to an equilibrium sound speed of 65% of the frozen sound speed. The assumptions of negligible particle volume fraction (dilute) and particle-particle collisions (disperse) begin to breakdown in the vicinity of this loading factor. The Prandtl number controls the relative equilibrium of the two phases between the momentum and heat transfer rates. A unit Prandtl number indicates that momentum and heat transfer occurs at similar rates. Small Prandtl numbers corresponds to a system that will reach temperature equilibrium much quicker than that of momentum. Conversely, a large Prandtl number corresponds to a system that will reach momentum equilibrium much quicker than that of

temperature. Therefore, the dispersion relationships were calculated for each of the loading factors listed above for Prandtl numbers of $Pr = 1$, $Pr = 10^{-3}$, and $Pr = 10^3$ and are plotted in Figs. 1(a), 2(a) and (b), respectively. The arrows indicate the direction of change from the frozen limit (high frequency) to the equilibrium limit (low frequency).

Due to the symmetry of the pair of acoustic modes in the imaginary axis, only one of the acoustic modes are shown in the dispersion relationship figures. As indicated previously in Eq. (24), four zero wave-speeds and two acoustic modes exist in the frozen limit. Two of the zero wave-speed modes remain undamped for all solution frequencies and are associated with convective transport of the gas and particle-phase densities. The other two zero wave-speed modes are also convective modes associated with the transport of differences in the velocities and temperatures of the two phases. These two modes are undamped in the frozen limit but are highly attenuated in the equilibrium limit. This is confirmed by the equilibrium wave solution determined previously, Eq. (21), where the gas and solid phases achieve equal velocity and temperature. The attenuation rates for the two damped and acoustic modes as a function of the solution wave length are plotted in Fig. 1(b) for a unit Prandtl number. This plot shows that the two purely damped modes quickly become highly damped as the wavelength increases (frequency decreases). The acoustic modes have finite damping for more intermediate solution frequencies and become undamped once again as the non-equilibrium frozen limit is reached. The zero damping of the acoustic modes in both the equilibrium and frozen limit is clearly depicted in

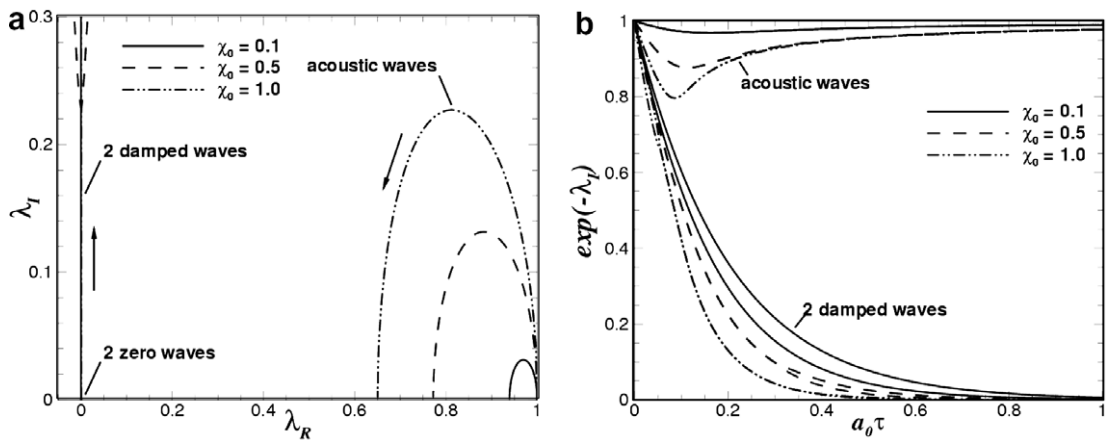


Fig. 1. (a) Dispersion relationship and (b) attenuation rates for a Prandtl number of unity, Pr , with various loading factors.

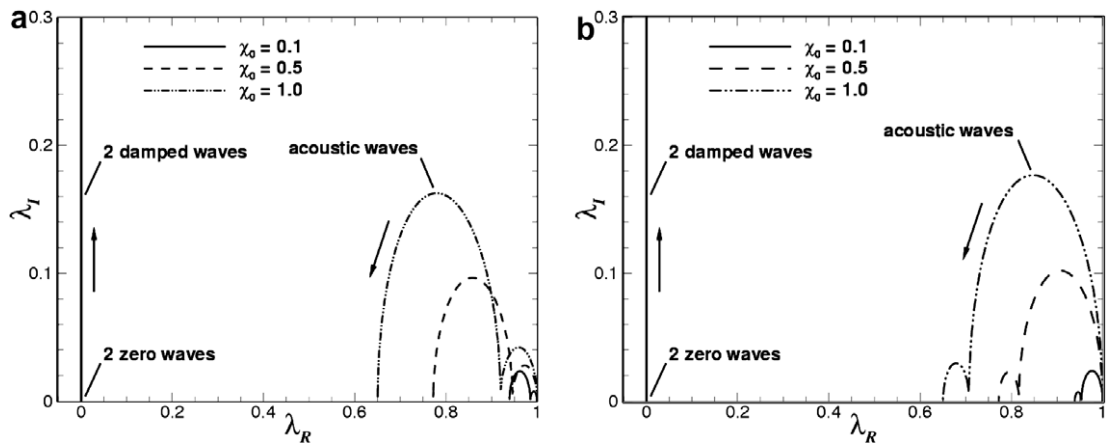


Fig. 2. Dispersion relationships for Prandtl numbers of (a) $Pr = 10^{-3}$ and (b) $Pr = 10^3$ with various loading factors.

Fig. 1(b) for a unit Prandtl number. It is seen in Fig. 2(a) for a system nearly in temperature equilibrium that an intermediate temperature equilibrium value of the acoustic wavespeed (with finite damping) occurs before the system reaches full equilibrium. Similarly, as shown in Fig. 2(b) for a system nearly in momentum equilibrium an intermediate momentum equilibrium value of the acoustic wavespeed (with finite damping) occurs before the system reaches full equilibrium.

The preceding dispersion analysis provides a complete description of how the two-phase flow equations progress from a degenerate hyperbolic system in the frozen limit to a strictly hyperbolic system in the equilibrium limit. This more complete picture of the degenerate nature of the Eulerian description was helpful in formulating the numerical approach described in the next section that alleviates issues associated with the degeneracy. Note also the interleaving of the non-equilibrium acoustic wave speeds between the frozen and equilibrium limits. This ensures that the frozen acoustic wavespeeds are the maximum attainable wavespeed. Therefore, in spite of the existence of the degeneracy in the non-equilibrium limit, stable solutions of the two-phase flow equations using upwind numerical schemes are attainable.

3. Numerical algorithm

3.1. Finite-volume scheme

In a finite-volume approach, the governing equations are solved in integral form over a domain discretized into computational cells and, therefore, naturally enforce conservation of the required solution quantities, such as mass, momentum, and energy. Upwind finite-volume schemes for the equations of compressible gas-dynamics were originally introduced by Godunov (1959). Application and development of these schemes for the gas dynamic equations has been well documented in literature. Refer to the recent textbooks by Hirsch (1990), Laney (1998), and Toro (1999) for a further details.

An explicit higher-order Godunov-type finite-volume scheme is used to solve the gas-particle equations of interest here (Sachdev et al. (2005a)). In this work, the governing equations are integrated over quadrilateral cells of a structured multi-block quadrilateral mesh. The preceding finite-volume procedure applied to cell (i, j) results in the following system of semi-discrete ordinary differential equations:

$$\left. \frac{d\mathbf{U}}{dt} \right|_{ij} = -\frac{1}{A_{ij}} \sum_k \vec{\mathbf{F}}_{ijk} \cdot \hat{n}_k \Delta l_k + \mathbf{P}_{ij}, \quad (26)$$

where A_{ij} is the area of cell (i, j) , Δl_k is the length of the cell face k , and \hat{n}_k is the unit vector normal to the cell face k . The vector \mathbf{U} represents the cell-averaged conserved variable solution vector,

$$\mathbf{U} = [\rho, \rho v_x, \rho v_y, E, \sigma_p, \sigma_p u_x, \sigma_p u_y, \epsilon_p]^T, \quad (27)$$

where v_x and v_y are the Cartesian components of the gas velocity \vec{v} and u_x and u_y are the Cartesian components of the particle velocity \vec{u} . The dyadic quantity $\vec{\mathbf{F}} = [\mathbf{F}_x, \mathbf{F}_y]$ is the flux dyad with components in the \hat{i} and \hat{j} directions

$$\mathbf{F}_x = [\rho v_x, \rho v_x^2 + p, \rho v_x v_y, v_x(E + p), \sigma_p u_x, \sigma_p u_x^2, \sigma_p u_x u_y, u_x \epsilon_p]^T, \quad (28)$$

$$\mathbf{F}_y = [\rho v_y, \rho v_x v_y, \rho v_y^2 + p, v_y(E + p), \sigma_p u_y, \sigma_p u_x u_y, \sigma_p u_y^2, u_y \epsilon_p]^T, \quad (29)$$

and the vector \mathbf{P} contains the gas-particle interaction source terms,

$$\mathbf{P} = \left[0, -\frac{\sigma_p}{\tau_v} (v_x - u_x), -\frac{\sigma_p}{\tau_v} (v_y - u_y), -\frac{\sigma_p}{\tau_v} (\vec{v} - \vec{u}) \cdot \vec{u} - \frac{\sigma_p c_p}{\tau_T} (T - T_p), \right. \\ \left. 0, \frac{\sigma_p}{\tau_v} (v_x - u_x), \frac{\sigma_p}{\tau_v} (v_y - u_y), \frac{\sigma_p c_p}{\tau_T} (T - T_p) \right]^T. \quad (30)$$

The inviscid numerical fluxes at the faces of each cell are determined from the solution of a Riemann problem. Given the left and right initial conditions, \mathbf{U}_l and \mathbf{U}_r , at the cell interfaces, the numerical flux is given by

$$\vec{\mathbf{F}} \cdot \hat{n} = \mathcal{F}(\mathbf{U}_l, \mathbf{U}_r, \hat{n}), \quad (31)$$

where \mathcal{F} is evaluated by solving a Riemann problem in a direction defined by the normal to the face, \hat{n} . The left and right initial states are determined using the least squares piece-wise limited linear solution reconstruction procedure of Barth (1993). The modified limiter of Venkatakrishnan (1993) has also been implemented.

Frozen flow conditions are assumed for the solution of the Riemann problem. In the frozen flow limit the phase interactions terms vanish and the gas and particle-phases fully decouple. Hence, separate Riemann problems and solutions can be formulated for the two phases. For the gas-phase, the efficient exact Riemann solver of Gottlieb and Groth (1988), the approximate Riemann solver of Roe (1981), and various average-state approximate Riemann solvers (Einfeldt (1988), Toro et al. (1994), Linde (2002)) have all been implemented. Solvers for the solution of the particle-phase Riemann problem, both single- and multi-velocity formulations are discussed in the next sub-section.

For time-accurate calculations, predictor–corrector time-marching methods are used to integrate the set of ordinary differential equations that result from the spatial discretization of the governing equations. The optimally smoothing multi-stage schemes developed by van Leer et al. (1989) are adopted for steady-state calculations. An estimation of the maximum allowable time-step is given by

$$\Delta t = \min \left[\beta \min \left(\frac{\Delta y}{|v_x| + a}, \frac{\Delta x}{|v_y| + a}, \frac{\Delta y}{|u_x|}, \frac{\Delta x}{|u_y|} \right), \beta_p \min(\tau_T, \tau_v) \right], \tag{32}$$

where β is the CFL-number used to ensure stability of the time-stepping scheme and β_p is used to restrict the time-step to be a multiple of the particle-relaxation time-scale.

3.2. Particle-phase Riemann problem

3.2.1. Single-velocity formulation

Determination of the flux values at cell interfaces for the particle-phase is complicated by the degeneracy of the governing flow equations described above. A particle-phase Riemann solver for a single-velocity formulation was proposed by Saurel et al. (1994). This flux function is now briefly reviewed and its limitations discussed.

Given the left and right particle-phase initial conditions defined by $\mathbf{W}_l = [\sigma_{p_l}, u_l, T_{p_l}]^T$ and $\mathbf{W}_r = [\sigma_{p_r}, u_r, T_{p_r}]^T$ three particle expansion wave configurations ($u_l < u_r$) and three particle compression wave configurations ($u_l > u_r$) were identified by Saurel et al. and used to construct solutions to the Riemann problem. Refer to Fig. 3. For the expansion configuration, if $u_l, u_r > 0$ then the interface solution provided by the solution of

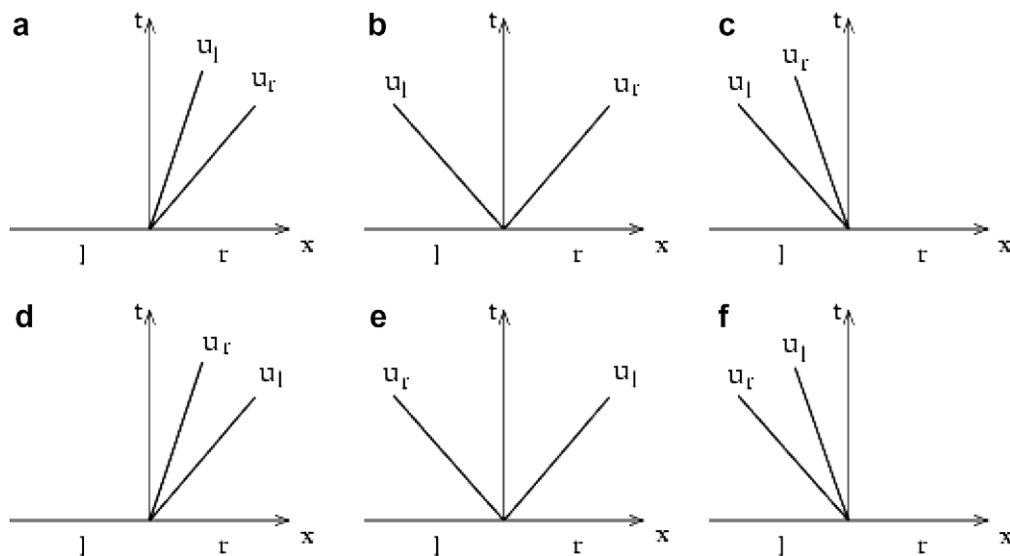


Fig. 3. The six possible wave patterns for the solution of the particle-phase Riemann problem (Saurel et al., 1994).

the Riemann problem is simply the left state. If $u_l, u_r < 0$ then the interface solution state is given by the right state. A strong expansion occurs when $u_l < 0$ and $u_r > 0$. In this case, the particles of the left and right states are moving apart in opposite directions, leaving a vacuum state at the interface.

For the compressive configurations ($u_l > u_r$), if $u_l, u_r > 0$ then the interface solution for the Riemann problem is the left state and if $u_l, u_r < 0$ the solution state is the right state. A strong compression of the particles occurs when $u_l > 0$ and $u_r < 0$. In the proposed Riemann solver of Saurel et al., the solution state in this last case is taken by $\sigma_p^* = \sigma_{p_l} + \sigma_{p_r}$, $u^* = (\sigma_{p_l} u_l + \sigma_{p_r} u_r) / \sigma_p^*$, and $T_p^* = (\sigma_{p_l} T_{p_l} + \sigma_{p_r} T_{p_r}) / \sigma_p^*$.

In all three of the compressive cases, the interface solution compromises the actual physics of the particle motions. For the mildly compressive cases where one solution state is catching up with the other, the solution information carried by the overtaken particles is partially lost. In reality, this solution information should be retained. For the more strongly compressive case, the two waves (populations of particles) should simply pass through each other. Instead, the particle concentrations are directly summed and density weighted averages are assigned to the particle velocity and temperature. An example of two crossing particle jets predicted using this single-velocity formulation is shown in Fig. 4(a). The particle jets are crossing at an angle of 45° . Vacuum conditions are assumed to exist in the channel and so the phase-interaction terms can be neglected. Although this averaging procedure provides the correct average state for the combined left and right moving particle populations, it fails to recognize the presence of the two oppositely moving populations and solution content is lost and not retained in the numerical approximation of the solution. A single particle jet is formed with no transverse momentum. This loss of information can lead to the unphysical results and difficulties near solid boundaries as described by Saurel et al. and by Slater and Young (2001) and is a basic limitation of any single-velocity particle-phase Eulerian formulation.

3.2.2. Multi-velocity formulation

To alleviate the issues involved with compression waves that occur when using a single-velocity formulation a multi-velocity treatment of the particle-phase is proposed in which the particle-field is split up into distinct velocity families and are advected separately in the flow. For two-dimensional flow, the particle-phase is decomposed into four distinct velocity families, with velocities in the north-east ($u_x > 0, u_y \geq 0$), north-west ($u_x \leq 0, u_y > 0$), south-west ($u_x < 0, u_y \leq 0$), and south-east ($u_x \geq 0, u_y < 0$) directions of velocity space. Eight velocity families would be required for three-dimensional flow.

Each family of particles are assigned their own mass, momentum, and energy and, therefore, are governed by their own equations of motion. The flux at cell interfaces is determined individually for each particle-family using a simplified version of the single-velocity formulation particle-phase Riemann solver of Saurel et al. Crossing particle trajectories are inherently accounted for in this approach as seen by the particle-phase streak-lines in Fig. 4(b) for two-impinging jets (interaction with the gas-phase is neglected). Moreover, reflection boundary conditions can be realistically modelled by simply reflecting the particle-phase to the appropriate particle family. For example, as shown in Fig. 4(b), a particle-wave travelling in the south-east direction perfectly reflects at the solid lower boundary and continues travelling in the north-east direction

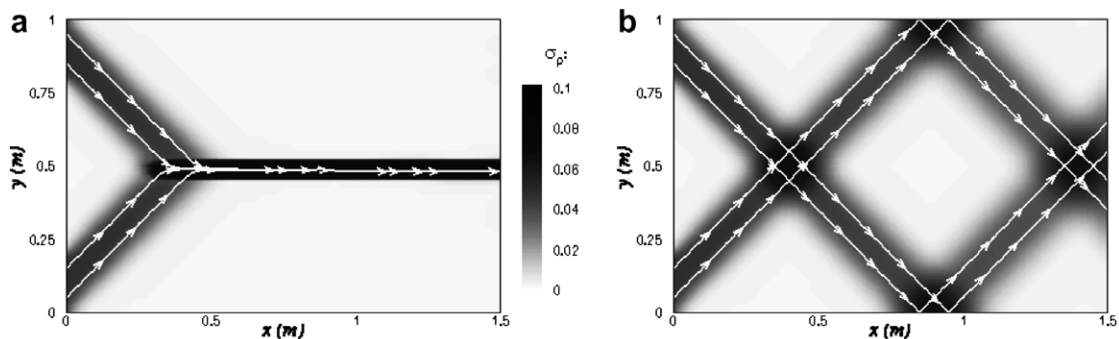


Fig. 4. Numerical prediction of the particle-phase concentration contours and streak-lines for two impinging particle jets in a vacuum using single-velocity (a) and multi-velocity (b) formulations.

without losing mass, momentum, or energy. It should be noted that the particle concentration contours plotted in Fig. 4(b) are for the total concentration found by summing the concentrations of all four two-dimensional flow particle velocity families.

Switching of the particle-phase velocity family can also be required due to the momentum phase interaction with the gas-phase as the system tends towards equilibrium. In this case, a particle-wave travelling in a different direction than the gas-phase may eventually be pulled into a different velocity family. To allow for this, the particle state for each family is averaged into the appropriate family in every computational cell of the mesh after each stage of the time-stepping scheme as required. A mass average is used, thereby enforcing conservation of mass, momentum, and energy. However, it should be noted that some solution content can be lost in the averaging process. An illustration of the change of velocity family due to momentum transfer is provided in Fig. 5 for a one-dimensional problem which involves two velocity families (left and right travelling). Initially, at t_0 a sine-squared particle-wave is travelling at uniform velocity in the opposite direction of the gas-phase which is travelling to the right at Mach 0.5 and is contained in the left-travelling velocity family. Due to drag, the system will relax into an equilibrium state in which both phases have the same momentum. At t_1 it is seen that the particle wave has slowed down but is still associated with the left-travelling velocity family. As soon as the velocity of the particle wave switches from negative to positive, approximately at t_2 the particle state is mass-averaged into the right-travelling velocity family and the left-travelling velocity family is deleted. The particle-wave then continues to relax into an equilibrium state as seen from times t_3 and t_4 .

A limitation of the multi-velocity treatment and the averaging approach described above is that although crossing particle trajectories can be accurately modelled, weakly compressive particle-phase flows with one particle-wave overtaking a slower particle-wave will produce one average wave, as found in the single-velocity formulation. This method also requires some additional computing resources in terms of both memory and computing time. However, stronger particle compression waves are easily reproduced and, therefore, crossing trajectories and reflection boundary conditions can be realistically handled.

3.3. Parallel adaptive mesh refinement

Adaptive mesh refinement (AMR) techniques which automatically adapt the computational grid to the solution of the governing partial differential equations can be very effective in treating problems with disparate length scales. A description of the block-based approach used here was provided by Sachdev et al. (2005a) and has been successfully applied to laminar and turbulent diffusion flames (Northrup and Groth, 2005; Gao and Groth, 2006), micron-scale flows (McDonald and Groth, 2005), and multi-phase rocket motor core flows (Sachdev et al., 2005a,b).

In this work, the governing equations are integrated to obtain area-averaged solution quantities within quadrilateral computational cells and these cells are embedded in structured blocks consisting of $N_x \times N_y$ cells, where N_x and N_y are even, but not necessarily equal integers. Solution data associated with each block are stored in indexed array data structures and it is therefore straightforward to obtain solution information from neighbouring cells within blocks. Mesh adaptation is accomplished by the dividing and coarsening of

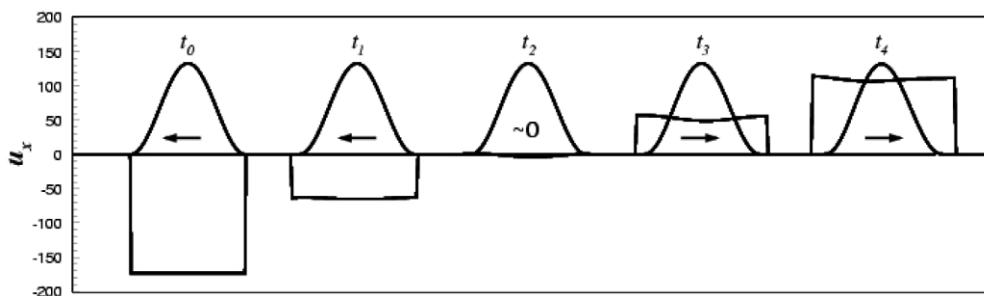


Fig. 5. Illustration of the change in velocity families due to momentum transfer between the two phases for a particle-wave with a sine-squared concentration distribution. The particle-wave is initially moving in the opposite direction of the gas-phase.

appropriate solution blocks. In regions requiring increased cell resolution, a “parent” block is refined by dividing itself into four “children” or “offspring”. Each of the four quadrants or sectors of a parent block becomes a new block having the same number of cells as the parent and thereby doubling the cell resolution in the region of interest. This process can be reversed in regions that are deemed over-resolved and four children are coarsened into a single parent block. The mesh refinement is constrained such that the grid resolution changes by only a factor of two between adjacent blocks and the minimum resolution is not less than that of the initial mesh. Standard multi-grid-type restriction and prolongation operators are used to evaluate the solution on all blocks created by the coarsening and division processes, respectively. In our previous work, the coarsening and division of blocks are directed using multiple physics-based refinement criteria. In this work, blocks containing disparate particle concentrations (areas of zero concentration or peaks) are flagged for division and blocks with constant particle concentration are flagged for coarsening. This refinement criteria allows for computational blocks to be clustered at areas of interest with respect to the particle-phase. An example of the application of the parallel AMR scheme to a gas-particle flow is described in Section 4.2.

A hierarchical tree-like data structure with multiple “roots”, multiple “trees”, and additional interconnects between the “leaves” of the trees is used to keep track of mesh refinement and the connectivity between solution blocks. This interconnected “forest” data structure is depicted in Fig. 6. The blocks of the initial mesh are the roots of the forest which are stored in an indexed array data structure. Associated with each root is a separate “quadtree” data structure that contains all of the blocks making up the leaves of the tree created from the original parent blocks during mesh refinement. One of the advantages of the hierarchical quadtree data structure is that it readily permits local mesh refinement. Local modifications to the multi-block mesh can be performed without re-gridding the entire mesh and re-calculating solution block connectivity.

Although the block-based AMR approach described above is somewhat less flexible and incurs some inefficiencies in solution resolution as compared to a cell-based approaches (i.e., for the same solution accuracy, generally more computational cells are introduced in the adapted grid), the block-based method offers many advantages over cell-based techniques when parallel implementation of the solution algorithm is considered and computational performance issues are taken into account. In particular, the multi-block quadrilateral mesh and quadtree data structure lends itself naturally to domain decomposition and thereby enables efficient and scalable implementations of the solution algorithm for the multi-phase flow equations on distributed-memory multi-processor architectures. A description of the parallel implementation of the algorithm was given by Sachdev et al. (2005a). An estimate of the relative parallel speed-up and efficiency of the algorithm is given in Fig. 7 for a fixed size problem involving the crossing particle jets discussed in the previous subsection which is performed gain in the next section with phase-interaction. It can be seen that the algorithm is nearly 100% efficient over 64 processors.

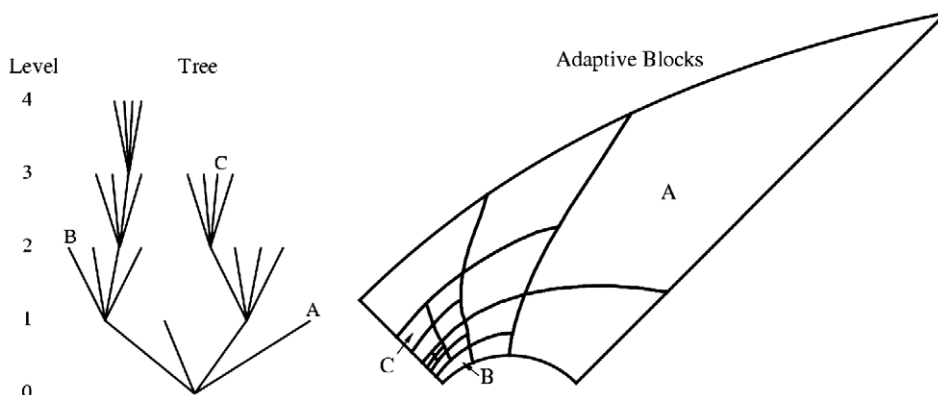


Fig. 6. Solution blocks of a computational mesh with four refinement levels originating from one initial block and the associated hierarchical quadtree data structure. Interconnects to neighbours are not shown.

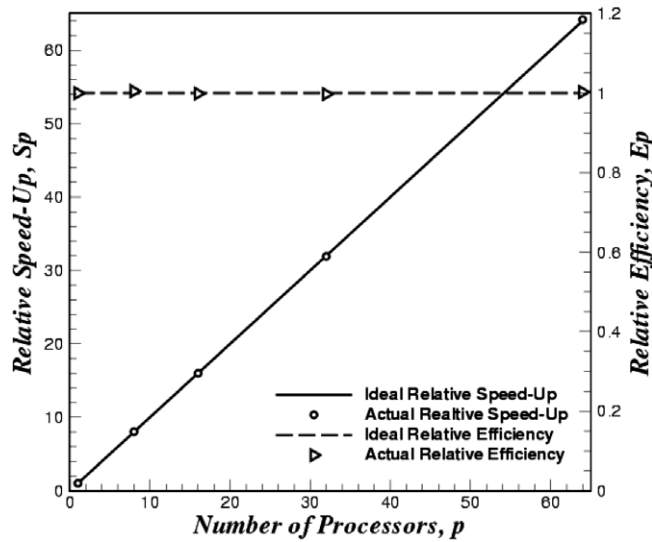


Fig. 7. Relative parallel speed-up, $S_p = (t_1/t_p)p$, and efficiency, $E_p = S_p/p$, for a fixed-size problem with 64 blocks and 55,296 cells (36×24) using up to 64 processors.

4. Numerical examples

4.1. Crossing particle jets

In Section 3.2 a problem involving two impinging particle jets was used to demonstrate the ability of the multi-velocity formulation to accurately predict such flows. Here, the same problem is considered while including the effects of the phase-interaction terms. Initially, the channel contains a uniform quiescent gas at atmospheric conditions with zero particle concentration. As done previously, the particle jets enter at the top and bottom of the channel at a 45° angle from the walls at a speed of 80% of the gas-phase sound speed, $|\vec{u}| = 0.8a$. Reflective boundary conditions are applied at the top and bottom surfaces of the channel walls. Fixed and constant extrapolation boundary conditions are used at the left and right boundaries of the domain, respectively. The computation is performed using both the single- and multi-velocity formulations and the results are plotted in Figs. 8 and 9 at 16.5 ms and 43 ms, respectively. Particle-phase concentration contours and streamlines are shown.

As shown in Fig. 8, the prediction of the the particle-phase concentration by both formulations is nearly identical soon after the collision of the particle-jets. However, the multi-velocity formulation demonstrates

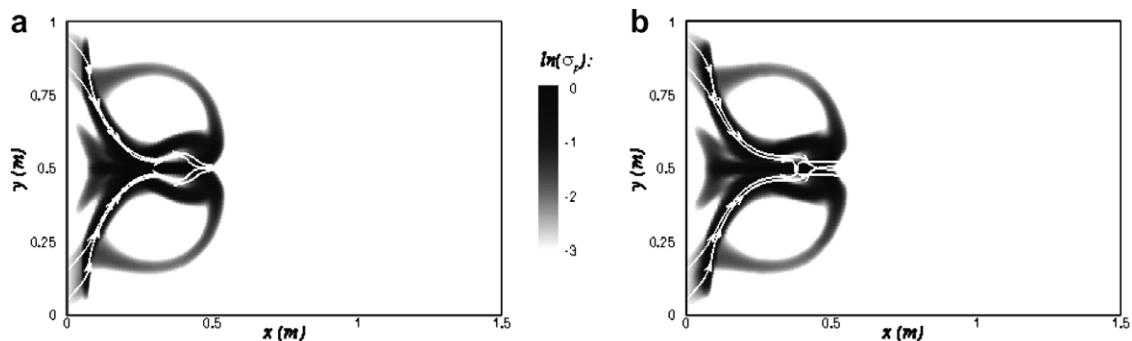


Fig. 8. Numerical prediction of the particle-phase concentration contours and streak-lines for two impinging particle jets in a quiescent gas at $t = 16.5$ ms using single-velocity (a) and multi-velocity (b) formulations.

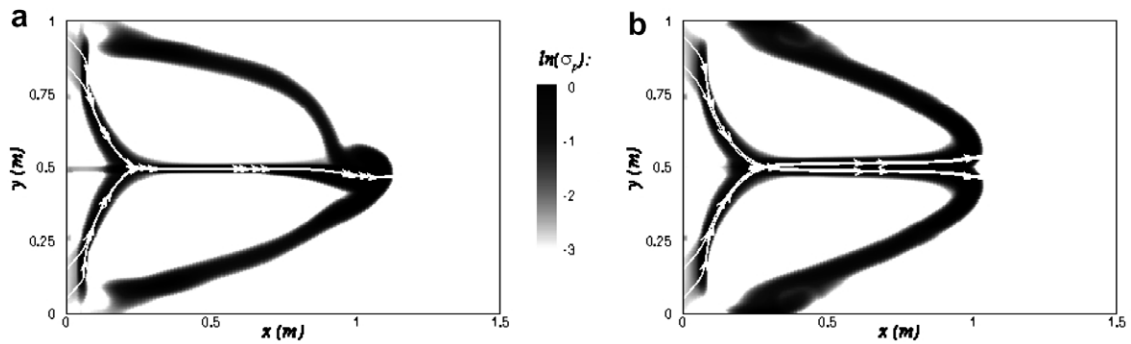


Fig. 9. Numerical prediction of the particle-phase concentration contours and streak-lines for two impinging particle jets in a quiescent gas at $t = 43$ ms using single-velocity (a) and multi-velocity (b) formulations.

a definite crossing of the particle-phase streamlines that is absent from the single-velocity formulation. Moreover, the inability of the single-velocity formulation to allow the particle-phase streamlines to cross leads to an instability in the computation that is seen in Fig. 9. This instability is related to the mathematical properties of the Eulerian description and the numerical solution scheme. It has similarities to a Kelvin–Helmholtz instability in fluid dynamics. It is experienced only when using a higher-order scheme and is a result of the higher-order reconstruction in areas with strong shear layers in the particle-phase. The multi-velocity formulation does not experience this instability since shear layers for each velocity family are avoided and the impinging jets simply pass through each other, thereby providing a symmetric solution. It should be noted that the multi-velocity formulation requires some additional computing resources in terms of both memory (12 additional variables) and approximately one-and-a-half times the computing time of the single-velocity formulation.

4.2. Solid propellant rocket motor flow

Predictions of solid propellant rocket motor operation for a configuration typical of a CRV-7 rocket system are now described to demonstrate the viability and capability of the proposed multi-velocity formulation for computing practical multi-phase flows. The CRV-7 rocket system contains a non-aluminized propellant composed of 80% oxidizer (ammonium perchlorate, AP) and 20% fuel (hydroxyl terminated polybutadiene, HTPB). As is typical in some tactical rocketry, inert aluminium oxide particles account for 3% of the solid propellant by mass. Therefore, the modelling of burning particles, particle–particle collision processes (such as agglomeration), and the transport of smoke are not required for the present work. In addition, the propellant ignition is assumed to be instantaneous and the burning rate dependent only on the local pressure as given by the empirical St. Robert relation (Kuo and Summerfield, 1986), $r_{bs} = 0.5[p(\text{kPa})]^{0.33}$ mm/s. The burning of the solid propellant and production of the propellant gases at the surface of the propellant grain is specified through the solution of a Riemann problem as described by Sachdev et al. (2005a). The treatment of the burning propellant boundary is very similar in spirit to the methods proposed by Gottlieb and Groth (1999) for imposing boundary data at a variety of flow boundaries based on the solution of Riemann problems.

Rocket motor predictions using the multi-velocity formulation are presented in Figs. 10–12 for a cylindrical grain rocket motor with a 40 mm internal radius, a nozzle throat radius of 10 mm, and an internal port radius of 20 mm. The propellant and particle characteristics are given in Table 2. The solution procedure involved time-stepping the conservation equations to steady-state then refining the mesh and computing again. This is repeated for four mesh refinements. The initial and final grid configurations are shown in Fig. 10 in the upper and lower panel of the figure, respectively. Note that only the nozzle end of the rocket is shown. The burning of the solid propellant leads to a head end pressure in excess of 2.8 MPa and produces sonic flow conditions at the nozzle throat and supersonic outflow in the rocket nozzle with the Mach number approaching 3.35. The particle-phase concentration contours through the converging-diverging nozzle computed using the multi-velocity formulation are depicted in Fig. 11 for the initial and final meshes in the upper and lower

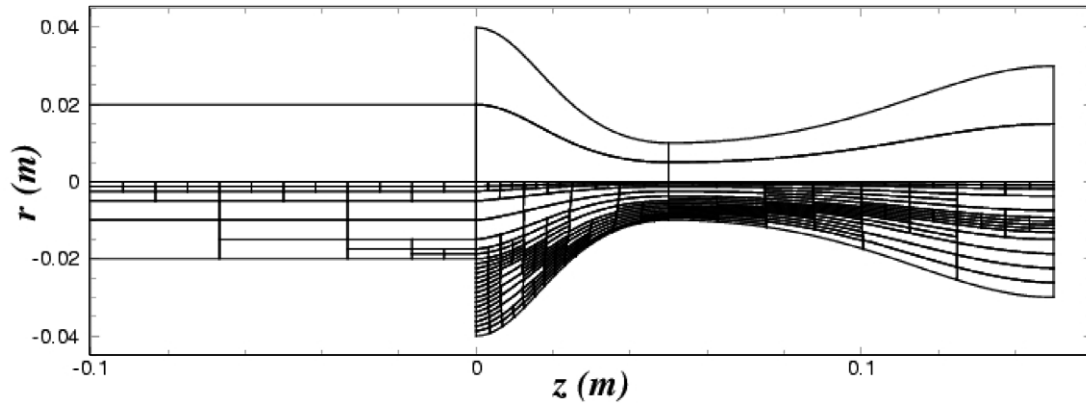


Fig. 10. Multi-block grid structure for a cylindrical grain rocket motor. The initial grid (upper panel) contains seven blocks and 2688 cells (24×16) and the final grid (lower panel) after four refinements contains 556 blocks and 213,504 cells. Entire rocket not shown.

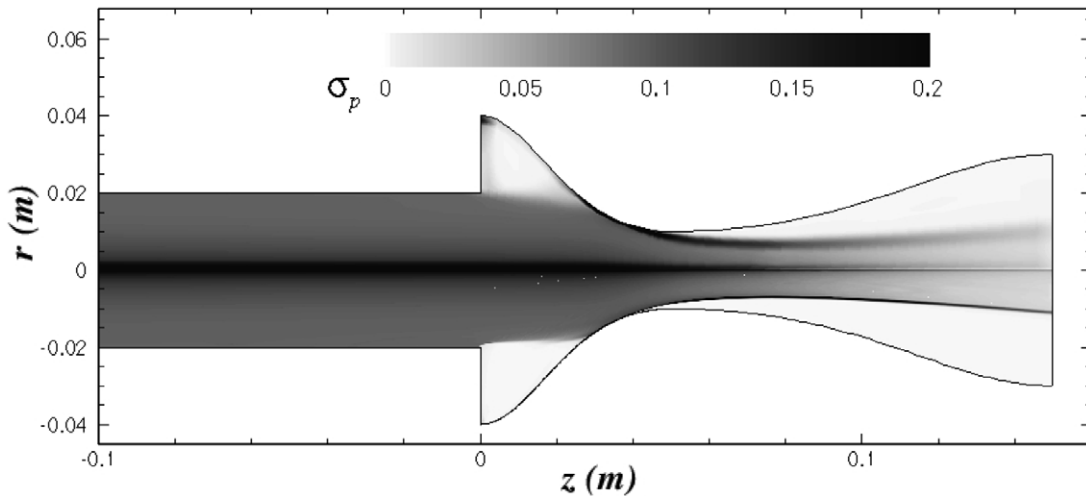


Fig. 11. Predicted particle-phase concentration contours for a cylindrical grain rocket motor calculated on the initial grid (upper panel) and the grid after four mesh refinements (lower panel).

portions of the figures, respectively. A comparison of the propellant gas and inert particle axial velocity components is shown in Fig. 12.

It is clear from Fig. 12 that the particle-phase velocity lag relative to the gas-phase velocity after the rapid acceleration through the nozzle is represented in this figure. The particles are unable to expand in the nozzle due to their relative high mass, resulting in a region of zero particle concentration in the diverging section of the nozzle as shown in Fig. 11. Before the nozzle throat, the particles are unable to negotiate the curvature of the converging section of the nozzle and impact the nozzle at a high velocity and can lead to erosion of the nozzle material. The particles become entrained with the gas and are pulled through the nozzle throat into the diverging section where a dense stream of particles can be seen. Similar results are found when using a single-velocity formulation for the particle-phase, however, with artificially higher peak concentrations predicted at the nozzle and the axis of symmetry due to issues associated with the degeneracy of the Eulerian formulation. The computations of Vuillot et al. (1997) and York et al. (2001) show similar patterns in the particle concentration contours. It can be seen in Fig. 11 that the application of the block-based mesh refinement algorithm has successfully clustered computational blocks at areas of interest. In particular, accurate resolution of the interface between zero and non-zero particle concentrations has been achieved.

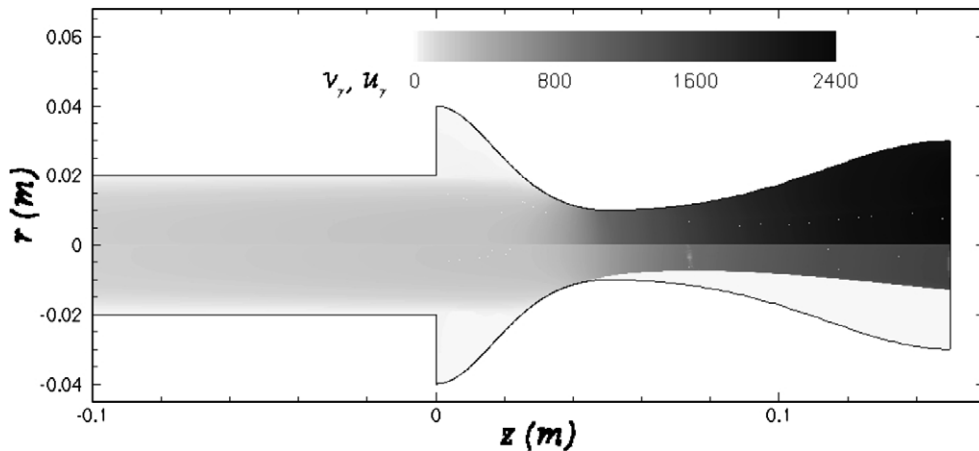


Fig. 12. Axial velocity component for the propellant gas-phase (upper panel) and inert particle-phase (lower panel) for a cylindrical grain rocket motor.

Table 2
Characteristics of the rocket propellant and the propellant combustion products

Propellant		Combustion products	
Density (ρ_s)	1740 kg/m ³	Specific gas constant (R)	318 J/kg K
Specific heat (c_s)	1510 J/kg K	Gas ratio of specific heats (γ)	1.21
Flame temperature (T_f)	3060 K	Gas absolute viscosity (μ)	8.19×10^{-5} kg/ms
Surface temperature (T_s)	1130 K	Gas thermal conductivity (κ)	0.184 W/m K
		Average particle diameter (d_p)	10 μ m
		Particle solid density (ρ_p)	2700 kg/m ³
		Particle specific heat (c_m)	900 J/kg K

5. Discussion and concluding remarks

A multi-velocity Eulerian formulation for predicting inert, disperse, and dilute gas-particle flow has been described. Though this method requires some additional computing resources in terms of both memory and computing time than single-velocity formulations, particle compression waves are permitted and, therefore, crossing trajectories and reflection boundary conditions can be modelled more realistically. In addition, this improved Eulerian formulation provides some advantages over a Lagrangian approach in terms of memory usage and ease of parallelization. Use of the block-based adaptive mesh refinement scheme in conjunction with the multi-velocity formulation for the particle-phase allows for accurate resolution of the flow structure of the particle-phase while minimizing computational resources and provides a natural domain decomposition for efficient parallel implementation. Future work will include application of this approach to the prediction of more realistic three-dimensional turbulent multi-phase rocket motor core flows.

Acknowledgements

This research was supported by a Premier's Research Excellence Award from the Ontario Ministry of Energy, Science, and Technology and by the Natural Sciences and Engineering Research Council of Canada. Funding for the parallel computing facility used to perform the computations described herein was obtained from the Canadian Foundation for Innovation and Ontario Innovation Trust (CFI Project No. 2169). The authors are very grateful to these funding agencies for this support.

References

- Barth, T.J., 1993. Recent developments in high order k -exact reconstruction on unstructured meshes. AIAA Paper 1993-0668.
- Einfeldt, B., 1988. On Godunov-type methods for gas dynamics. *SIAM J. Numer. Anal.* 25, 294–318.
- Gao, X., Groth, C.P.T., 2006. Parallel adaptive mesh refinement scheme for turbulent non-premixed combustor flow prediction. AIAA Paper 2006-1448.
- Godunov, S.K., 1959. Finite-difference method for numerical computations of discontinuous solutions of the equations of fluid dynamics. *Mat. Sb.* 47, 271–306.
- Gottlieb, J.J., Groth, C.P.T., 1988. Assessment of Riemann solvers for unsteady one-dimensional inviscid flows of perfect gases. *J. Comput. Phys.* 78, 437–458.
- Gottlieb, J.J., Groth, C.P.T., 1999. Collection of boundary conditions for one- and some multi-dimensional unsteady flows of polytropic gases. *Can. Aeronaut. Space J.* 45, 161–182.
- Groth, C.P.T., Roe, P.L., Gombosi, T.I., Brown, S.L., 1995. On the nonstationary wave structure of a 35-moment closure for rarefied gas dynamics. AIAA Paper 1995-2312.
- Haider, A., Levenspiel, O., 1989. Drag coefficient and terminal velocity of spherical and nonspherical particles. *Powder Technol.* 58, 63–70.
- Hirsch, C., 1990. *Numerical Computation of Internal and External Flows: Computational Methods for Inviscid and Viscous Flows*, vol. 2. John Wiley & Sons, Toronto.
- Igra, O., Hu, G., Falcovitz, J., Wang, B.Y., 2004. Shock wave reflection from a wedge in a dusty gas. *Int. J. Multiphase Flow* 30, 1139–1169.
- Kuo, K.K., Summerfield, M., 1986. *Fundamentals of Solid Propellant Combustion*. Progress in Astronautics and Aeronautics, vol. 90. American Institute of Aeronautics and Astronautics.
- Laney, C.B., 1998. *Computational Gasdynamics*. Cambridge University Press, Cambridge.
- Linde, T., 2002. A practical, general-purpose, two-state HLL Riemann solver for hyperbolic conservation laws. *Int. J. Numer. Meth. Fluids* 40, 391–402.
- Marble, F.E., 1970. Dynamics of dusty gases. *Ann. Rev. Fluid Mech.* 2, 397–446.
- McDonald, J.G., Groth, C.P.T., 2005. Numerical modeling of micron-scale flows using the Gaussian moment closure. AIAA Paper 2005-5035.
- Najjar, F.M., Balachandar, S., Alavilli, P.V.S., Ferry, J., 2000. Computations of two-phase flow in aluminized solid propellant rockets. AIAA Paper 2000-3568.
- Northrup, S.A., Groth, C.P.T., 2005. Solution of laminar diffusion flames using a parallel adaptive mesh refinement algorithm. AIAA Paper 2005-0547.
- Patankar, N.A., Joseph, D.D., 2001a. Modeling and numerical simulation of particulate flows by the Eulerian–Lagrangian approach. *Int. J. Multiphase Flow* 27, 1659–1684.
- Patankar, N.A., Joseph, D.D., 2001b. Lagrangian numerical simulation of particulate flows. *Int. J. Multiphase Flow* 27, 1685–1706.
- Roe, P.L., 1981. Approximate Riemann solvers, parameter vectors, and difference schemes. *J. Comput. Phys.* 43, 357–372.
- Rudinger, G., 1980. *Fundamentals of Gas-Particle Flow*. Elsevier Scientific Publishing Company, Amsterdam.
- Sachdev, J.S., Groth, C.P.T., Gottlieb, J.J., 2005a. A parallel solution-adaptive scheme for predicting multi-phase core flows in solid propellant rocket motors. *Int. J. Comput. Fluid Dyn.* 19, 157–175.
- Sachdev, J.S., Groth, C.P.T., Gottlieb, J.J., 2005b. Parallel AMR scheme for turbulent multi-phase rocket motor core flows. AIAA Paper 2005-5035.
- Saito, T., Marumoto, M., Takayama, K., 2003. Numerical investigations of shock waves in gas-particle mixtures. *Shock Waves* 13, 299–322.
- Sauerwein, H., Fendell, F.E., 1965. Method of characteristics in two-phase flow. *Phys. Fluids* 8, 1564–1565.
- Saurel, R., Daniel, E., Loraud, J.C., 1994. Two-phase flows: second-order schemes and boundary conditions. *AIAA J.* 32, 1214–1221.
- Slater, S.A., Young, J.B., 2001. The calculation of inertial particle transport in dilute gas-particle flows. *Int. J. Multiphase Flow* 27, 61–87.
- Toro, E.F., 1999. *Riemann Solvers and numerical methods for fluid dynamics*. Springer-Verlag, Berlin.
- Toro, E.F., Spruce, M., Speares, W., 1994. Restoration of the contact surface in the HLL-Riemann solver. *Shock Waves* 4, 25–34.
- Turton, R., Levenspiel, O., 1986. A short note on the drag correlation for spheres. *Powder Technol.* 47, 83–86.
- van Leer, B., Tai, C.H., Powell, K.G., 1989. Design of optimally-smoothing multi-stage schemes for the Euler equations. AIAA Paper 1989-1933-CP.
- Venkatakrishnan, V., 1993. On the accuracy of limiters and convergence to steady state solutions. AIAA Paper 1993-0880.
- Vuillot, F., Basset, T., Dupays, J., Daniel, E., Lupoglazoff, N., 1997. 2D Navier–Stokes stability computations for solid rocket motors: rotational, combustion and two-phase flow effects. AIAA Paper 1997-3326.
- York, B.J., Lee, R.A., Sinha, N., Dash, S.M., 2001. Progress in the simulation of particulate interactions in solid propellant rocket exhausts. AIAA Paper 2001-3590.